

**LONG-LIVED NEUTRAL HADRONS
IN THE CALORIMETER OF THE ZEUS DETECTOR**

FARIDAH MOHAMAD IDRIS

**FACULTY OF SCIENCE
UNIVERSITY OF MALAYA
KUALA LUMPUR**

2011

**LONG-LIVED NEUTRAL HADRONS
IN THE CALORIMETER OF THE ZEUS DETECTOR**

FARIDAH MOHAMAD IDRIS

**THESIS SUBMITTED IN THE FULFILLMENT OF
THE REQUIREMENT FOR THE DEGREE
OF DOCTOR OF PHILOSOPHY**

**DEPARTMENT OF PHYSICS
FACULTY OF SCIENCE
UNIVERSITY OF MALAYA
KUALA LUMPUR**

2011

UNIVERSITI MALAYA

ORIGINAL LITERARY WORK DECLARATION

Name of Candidate: FARIDAH MOHAMAD IDRIS (I.C/Passport No: 651031-02-5788)

Registration/Matric No: SHC060001

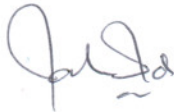
Name of Degree: DOCTOR OF PHILOSOPHY

Title of Project Paper/Research Report/Dissertation/Thesis ("this Work"):
LONG-LIVED NEUTRAL HADRONS IN THE CALORIMETER OF THE ZEUS DETECTOR

Field of Study: NUCLEAR AND PARTICLE PHYSICS

I do solemnly and sincerely declare that:

- (1) I am the sole author/writer of this Work;
- (2) This Work is original;
- (3) Any use of any work in which copyright exists was done by way of fair dealing and for permitted purposes and any excerpt or extract from, or reference to or reproduction of any copyright work has been disclosed expressly and sufficiently and the title of the Work and its authorship have been acknowledged in this Work;
- (4) I do not have any actual knowledge nor do I ought reasonably to know that the making of this work constitutes an infringement of any copyright work;
- (5) I hereby assign all and every rights in the copyright to this Work to the University of Malaya ("UM"), who henceforth shall be owner of the copyright in this Work and that any reproduction or use in any form or by any means whatsoever is prohibited without the written consent of UM having been first had and obtained;
- (6) I am fully aware that if in the course of making this Work I have infringed any copyright whether intentionally or otherwise, I may be subject to legal action or any other action as may be determined by UM.



Candidate's Signature

Date: 22.12.2010

Subscribed and solemnly declared before,

Witness's Signature



Date:

Name: PROF DR WAN AHMAD TAJUDDIN WAN ABDULLAH
Designation: DEAN, FACULTY OF COMPUTER SCIENCE AND
INFORMATION TECHNOLOGY, UNIVERSITY OF MALAYA

Witness's Signature



Date: 23.12.2010

Name: PROF DR ZAINOL ABIDIN IBRAHIM
Designation: LECTURER, PHYSICS DEPARTMENT,
FACULTY OF SCIENCE, UNIVERSITY OF MALAYA

ABSTRACT

During the electron-proton collision at HERA, the long-lived neutral hadrons in their final states may travel from the centre of the ZEUS detector to reach the calorimeter and deposit its energy in the calorimeter as islands of energies. The neutral hadrons travel in straight path and were not deflected by the magnetic field in the ZEUS detector.

In this thesis, measurements of the long-lived neutral hadrons K_L^0 and neutron in the final states in the calorimeter of the ZEUS detector has been carried out using the energy deposited by ZEUS Unidentified Flow Objects (ZUFOS) that were not associated with any tracks.. The kinematic variables of K_L^0 has been measured with virtual photon gain $0 < Q^2 < 150 GeV^2$ and centre-of-mass for intermediate boson-proton $W_{JB} = 25 GeV$. The reconstruction of invariant mass of vector meson $\phi(1020)$ using decay $\phi(1020) \rightarrow K_L^0 K_S^0$ and baryon Λ through decay channel $\Lambda \rightarrow n \pi^0$ has been carried out, with both showing good agreement with the standard invariant mass [35] of $\phi(1020)$ and Λ . The differential cross sections of $\phi(1020)$ and Λ and their respective daughter of K_L^0 and neutron with respect to their momentum were also calculated.

ACKNOWLEDGEMENT

I would like to thank and extend my gratitude to all the people involved in making this project a success.

First of all, I would like express my debt and gratitude to my supervisor Prof Dr Wan Ahmad Tajuddin Wan Abdullah and my co-supervisor Prof Dr Zainol Abidin Ibrahim, both of Jabatan Fizik, Unversiti Malaya, Kuala Lumpur, for their guidance, patience and support in the duration of this project.

I would also like thank ZEUS collaboration and Deutsches Electronen Synchrotron (DESY) for supporting this research project. I would also like thank my department Malaysian Nuclear Agency and Ministry of Science Technology and Innovation (MOSTI) of Malaysia for their support in this project.

For those whose name I do not mention here but have helped me in one way or another, please accept my sincere thank and gratitude. Thank you all very much.

PREFACE

In quest for knowledge, the endeavors put together by all parties to make a project undertaken a success is much more meaningful, than an individual alone. Such quest for the understanding the structure of matter to its most basic building block is an infinity. Save for the occasional tiredness of the mind and body, the hunger to understand more of nature's phenomena will perhaps push one's mind and capability towards excellence.

Thus, this project is dedicated to all mankind in pursuit of knowledge, may we be united by the knowledge that knowledge knows no boundaries.

TABLE OF CONTENTS

Chapter	Title	Page
Chapter 1	Introduction	1
Chapter 2	Theoretical Review	4
2.1	The Standard Model	4
2.2	Quark Parton Model (QPM)	6
2.3	Quantum Chromodynamics (QCD)	7
2.3.1	Perturbative Quantum Chromodynamics	8
2.4	String Fragmentation And The Lund string Model	8
2.5	Boson Gluon Fusion	10
2.6	Vector Meson $\phi(1020) \rightarrow K_0^L K_0^S$	11
2.7	Color Dipole Moment (CDM)	15
2.8	Kinematic Variables of the Electron-Proton Collision	18
2.9	Kinematic Variables of Hadrons in the Final States	20
2.9.1	Deep Inelastic Scattering (DIS)	25
2.10	Long Live Neutral Hadrons in Final States	26
2.10.1	K_L^0 Production	26
2.10.2	Neutron Production at HERA	28
2.10.3	Neutron Production through $\Lambda \rightarrow n\pi^0$ channel	30
2.11	Conservation of Strangeness Number	32
Chapter 3	The Zeus Experiment at HERA	
3.1	The HERA Storage Ring	35
3.2	The ZEUS Detector	38

3.2.1	The High Resolution Calorimeter	39
3.2.2	The Uranium-Scintillator	40
3.2.3	Calorimeter Layout	41
3.2.4	ZEUS Tracking Detector	44
3.2.4	Hadron Electron Separator (HES)	46
3.3	Calorimeter Tracking and ZUFOS	48
3.4	Monte Carlo and Event Simulation	49
3.4.1	Event Generators	51
3.4.1.1	Pythia	52
3.4.1.2	Ariadne	53

Chapter 4 Readout Control and Halomuons

4.1	CAL Readout control (ROC) of the ZEUS Detector	54
4.1.1	The Readout Controlling Modules	55
4.1.1.1	The Functions	55
4.1.2	FPGA programming	56
4.1.3	Coding with Verilog	57
4.1.4	FPGA Simulation and Results	60
4.1.5	FPGA-based ROC Power consumption	62
4.1.6	Hardware Development	63
4.1.7	Summary	66
4.2	The Halomuons in the ZEUS detector	67
4.2.1	Halomuons production upstream of ZEUS detector	68
4.2.2	The EMCs and HACs in F/RCALs	69

4.2.3	The Algorithm for halomuon analysis	70
4.2.4	Results	71
4.2.5	Summary	72

Chapter 5 Event selection and Reconstruction

5.2	Selection of K_L^0 and n candidates	80
5.2	Selection of K_S^0 candidates	84
5.3	Selection of Scattered electrons and photons in $e(k) p(P) \rightarrow e'(k') p'(P') X\gamma$ interaction	86
5.3.1	Selection of scattered electrons	86
5.4	Selection of Double Photon candidates from $\pi^0 \rightarrow \gamma\gamma$ decay	87
5.5	Reconstruction of $\phi(1020)$ from $\phi(1020) \rightarrow K_L^0 K_S^0$ channel	89
5.6	Reconstruction of Λ^0 from $\Lambda \rightarrow n\pi^0$ channel	89
5.7	Comparison with Monte Carlo Simulation	90
5.8	Defferential Cross Sections	91
5.9	Summary	92

Chapter 6 Result and Discussion

6.1	Reconstruction of $\phi(1020)$ mass from $\phi(1020) \rightarrow K_L^0 K_S^0$ channel	94
6.1.1	Reconstruction of K_L^0 kinematic variables	94
6.1.2	Background cuts	95
6.1.3	The four-momenta of K_L^0 candidates	96

6.1.4	Kinematic variables of K_L^0	99
6.1.5	Reconstruction of Scattered electrons in $e(k) p(P) \rightarrow e'(k') p'(P') X\gamma$ interaction	101
6.1.6	Reconstructed mass of K_L^0	105
	6.1.6.1 Cross section of K_L^0	109
6.1.7	Reconstruction of K_S^0 momentum	111
6.1.8	Reconstruction of $\phi(1020)$	113
	6.1.8.1 Cross section of $\phi(1020)$	115
	6.1.8.2 Correlation of $\phi(1020)$ with polar angles with K_L^0 , and K_S^0	117
6.2	Production of Λ from $\Lambda \rightarrow n\pi^0$ channel	119
6.2.2	Background cuts	119
6.2.3	The four-momenta of neutron candidates	120
6.2.4	Kinematic variables of neutron	123
6.2.5	Reconstructed mass of neutron	124
	6.2.5.1 Neutron azimuthal angle	125
	6.2.5.2 Differential cross section of neutron	126
6.2.6	Reconstruction of $\pi^0 \rightarrow \gamma\gamma$ candidates	128
6.2.7	Reconstruction of Λ	130
	6.2.7.1 Differential cross section of Λ	131
6.2.3	Summary	132

List of Figures

- Figure 2.1** Kinematic variables in the electron-proton collision, with P , k , q as them momentum of proton, electron, and photon respectively (generated in the process).
- Figure 2.2** Boson Gluon Fusion (BGF) diagram from a Deep Inelastic Scattering (DIS) of a lepton and hadron
- Figure 2.3** Electron-proton scattering at small Q^2 , with the electron as a source of virtual photon γ^* flux interacting with incoming proton resulting in hadronization of particle X in $\gamma^* p$ interaction
- Figure 2.4** Elastic vector meson production through Vector Dominance Model (VDM), with the photon fluctuating into a vector meson, which then scatters elastically from proton via the exchange of a pomeron [21]
- Figure 2.5** In the exclusive vector meson production based on the perturbative QCD model, the photon fluctuates into a $q\bar{q}$ pair, which then scatters off the proton to produce vector meson, via the exchange of two gluons (with momentum fraction x_1, x_2) [21]
- Figure 2.6** $SU(3)_{\text{flavor}}$ multiplets of light vector mesons, with various states classified by their strangeness content S and the third component I_3 of their isospin [31]
- Figure 2.7** Gluon emission g_2 from a $q\bar{q}$ pair in Color Dipole Moment (CDM) model, (a) gluon emission from quark (b) gluon emission from anti-quark [49]

Figure 2.7b Orientation of a dipole after emission. azimuthal angle ϕ of the emitted gluon and the polar angle θ of the incoming parton 1

Figure 2.8a Phase space limits for emission of the first gluon (thick lines) and available space for gluon emission (dash lines) in DIS [49]

Figure 2.9 Kinematic variables in the electron-proton collision, with P, k, q as the momentum of proton p , electron e , and photon γ respectively (generated in the process). The production of ϕ meson via a pomeron exchange and a virtual photon γ in the vector meson model (VDM)

Figure 2.10 Direction of a particle with four-momentum $p_i = (p_{xi}, p_{yi}, p_{zi}, E_i)$, with z-axis positive in the direction of the proton beam, x-axis positive in the HERA ring direction.

Figure 2.11 An exclusive ϕ decay through $\phi \rightarrow K_L^0 K_S^0$ channel (34.0% yield), where $K_S^0 \rightarrow \pi^+ \pi^-$ (69.2%)

Figure 2.12 Resolved One-Pion exchange diagram[37]

Figure 2.13a An Example of Λ^0 decay through $\Lambda^0 \rightarrow \pi^- p^+$ channel, where the two decay products moved apart in electromagnetic field in CTD., leaving two detectable tracks[7]. The yield is 63.9%

Figure 2.13b An Example of Λ^0 decay through $\Lambda \rightarrow n \pi^0$ channel (35.8% yield) where the two decay products moved along its original trajectories in two undetectable tracks, with $\pi^0 \rightarrow 2\gamma$ (98.8%)

Figure 3.1a HERA and PETRA accelerators aerial view at the DESY campus in Hamburg, HERA is at 10-20m underground with circumference 6.3km.

Figure 3.1b Schematic diagram of the HERA layout with ZEUS detector at south of HERA

Figure 3.2 Logitudinal cross section view of the Zeus detector [41]. The FCAL, BCAL and the RCAL forms the hadronic calorimeter of the ZEUS detector

Figure 3.3a Structure of a tower in a module of a Forward Calorimeter (FCAL) showing the uranium-scintillator sandwich (b) Sideview of a FCAL module . The uranium as passive material produced slow neutron to compensate losses of hadronic shower, while act as absorber to electromagnetic particles. The active scintillator SCSN-38 interact with slow neutrons from hadronic shower to produce signals for photomultiplier tube (PMT) via the wavelength shifter (WLS) [42][43]

Figure 3.4 Diagram of BCAL tower, with EMC cells backed 2 HAC cells (BCAL towers were projective in η and θ). The hadron particles, electromagnetic (e/m) particles and mouns shower differently in the calorimeter

Figure 3.5. A helix in XY plane, where ϕ is the outbound tangent angle in XY plane in the CTD [46]

Figure 3.6. Radial force distribution along the coil axis of the magnetic field in central tracking detector (CTD) [41]

Figure 3.7 CTD layout of the ZEUS detector [1]

Figure 3.8 Front and rear Hadron Electron Separator (HES) FHES and RHES respectively, in front of calorimeter in the ZEUS detector

Figure 3.9a The arrays 23 modules and 23 towers calorimeter in the ZEUS detector. Each cell (i,j) in the calorimeter in the calorimeter comprised of i-th module, j-th tower. The figure also shows 3 skis of the HES superimpose in front of the EMC [45]

Figure 3.9b Silicon pad (3cmx3cm) mounted on skis, map to one calorimeter cells [45]

Figure 3.10 Neutral ZUFOS move in straight trajectory from the interaction point through the EMC (electromagnetic calorimeter) to HACs (hadronic calorimeters) in the ZEUS detector, forming islands of energy deposits in the calorimeter. Neighboring cells were clustered to form cone clusters and matched to tracks [2].

Figure 3.11 Flow diagram of event analysis in the ZEUS detector. Simulated and actual events were run concurrent and compared to extract correction factor from pQCD calculation.

Figure 4.1 **Figure 4.1.** Schematic diagram of the calorimeter (CAL) read-out control of ZEUS detector with 96ns HERA clock for synchronization. See **Table 4.1** for parameters definition

Figure 4.2 The analogue modules of readout control (ROC) of the ZEUS detector were coded into single board, FPGA-based using Verilog before being simulated on Quartus II.

Figure 4.3. Coding sequence of the controlling analog read-out modules using Verilog. Coding were carried out starting with basic blocks, later combined to become the main controlling block

Figure 4.4 Two of the FPGA-based small sub-modules used in the table controlling block.

Figure 4.5 Full Quartus II RTL viewer of the FPGA-based readout control for the calorimeter of the ZEUS detector, showing the four main module i.e. pipeline, format, buffer and table, with inputs on the left and outputs on the right of the diagram.

Figure 4.6 Serial data input to the FPGA-based readout control (serial[0] for table control, serial[3] for pipeline, serial[5] for format control, serial[7] for generator control; while serial[0],[2],[4],[6] were serial clock 10MHz)

Figure 4.7a Output signals from the FPGA-based readout control

Figure 4.8b A close-up of the FPGA-based readout control showing the abort ABT signal from the pipeline control

Figure 4.9 A 7cm by 11cm PCB designed using Proteus software, with the FPGA Altera Cyclone mounted in the middle and TTL-ECL, ECL-TTL and Quad Bus Driver chips mounted fully. The PCB was tested in laboratory using frequency generator and high current voltage supply

Figure 4.10 Plot of current I_{CC} (A) and I_{EE} (A) versus number of chips of TTL-ECL quad translator type (MC0124) showing the tendency the currents to increase with the number of chips

Figure 4.11 Plot of current I_{CC} (A) and I_{EE} (A) versus number of chips of quad bus driver type (MC0192) showing the tendency the currents to increase with the number of chips

Figure 4.12 Plot of power (watt) from bias drain and emitter current and their total power versus number of chips of quad TTL-ECL quad translator type

Figure 4.13 Plot of power (watt) from bias drain and emitter current and their total power versus number of chips of quad bus driver type

Figure 6.1a Comparison of ZUFOS energy $zufe(4,i)$ for object- i not associated with any track (solid line) against its background signal (dash line); (b) the background signal is curve fitted using function $e^{(a+b*zufe(4,i))}$ and is then used to isolate the ZUFOS energy of K_L^0 candidates from its background signal

Figure 6.2 The four-momenta from ZUFOS entry for object- i not associated with any track (a) energy (GeV) of K_L^0 candidates and its associated momentum components (in GeV) (b) in x-direction (c) in y-direction (d) in z-direction assuming the particles as pions.

- Figure 6.3** Cosine polar angle of K_L^0 candidates (a) measured $\cos\theta$ and (b) $\cos\theta$ from Monte Carlo simulation
- Figure 6.4** Polar angles $\cos\phi$ of K_L^0 candidates
- Figure 6.5** Reconstructed momentum distribution of K_L^0 candidates (a) momentum of K_L^0 candidates (b) momentum in x-direction (c) momentum in y-direction (d) momentum in y-direction
- Figure 6.6** Transverse properties of K_L^0 candidates: (a) transverse energy (in GeV) (b) transverse momentum (in GeV) (c) $\delta_i = E_i - p_{zi}$ (in GeV)
- Figure 6.7a** Rapidity and (b) pseudorapidity of K_L^0 candidates
- Figure 6.8** Properties of reconstructed K_L^0 reconstructed candidates (a) Momentum gain from incoming electron $Q^2 = -(k - k')^2$; (b) $x_{JB} = \frac{Q^2}{s y_{JB}}$ as fraction of transferred proton momentum to a struck quark ;(c) centre-of-mass $W_{JB} = \sqrt{y_{JB} s}$, for the intermediate boson-proton
- Figure 6.9** Reconstructed momentum of scattered electron candidates from DIS (a) momentum of scattered electron with (b) in x-direction; (b) y-direction (c) in z-direction, using ZUFOS charge tracks in EMC of ZEUS detector
- Figure 6.10** Properties of reconstructed scattered electron candidates from DIS (a) polar angle θ in radian; (b) azimuthal angle ϕ in radian (c) energy (GeV); (d) virtual photon gain $Q^2 = -(k - k')^2$, using ZUFOS charge tracks in EMC of ZEUS detector
- Figure 6.11** Two dimensional plot of energy (GeV) of scattered electron candidates from DIS vs. $Q^2 = -(k - k')^2$.(GeV)²

Figure 6.11 Two dimensional plot of $Q^2 = -(k - k')^2$ vs centre-of-mass $W_{JB} = \sqrt{y_{JB} s}$ for the intermediate boson-proton

Figure 6.12 Two dimensional plot of $Q^2 = -(k - k')^2$ vs centre-of-mass $W_{JB} = \sqrt{y_{JB} s}$ for the intermediate boson-proton

Figure 6.13a Reconstructed mass in GeV of K_L^0 candidates, from ZUFO objects not associated with any tracks (b) an expansion of Figure (a) . The invariant mass of K^0 is 0.498GeV [35]

Figure 6.14 Reconstructed mass (in GeV) of K_L^0 candidates with errors. The invariant mass of K^0 is 0.498GeV

Figure 6.15 Comparison of mass of K_L^0 from Monte Carlo simulation (solid line) against reconstructed mass of K_L^0 candidates (dash line) in GeV on log scale.

Figure 6.16a Two dimensional plot of mass (GeV) vs $\cos\vartheta$ of K_L^0 at pseudorapidity $-2 < \eta < 2$ (ϑ as the polar angle of K_L^0)

Figure 6.17 Comparison of momentum (in GeV) of K_L^0 candidates (a) measured (b) matched against the ones generated from Monte Carlo and matched against measured momentum; (c) corrected

Figure 6.18 Comparison of (a) efficiency vs. energy (in GeV); (b) purity vs. energy (GeV); (c) acceptance vs. energy (GeV) of momentum of K_L^0 candidates

Figure 6.19 Differential cross section (in pb/GeV) of K_L^0 candidates with respect to its measured momentum (in GeV)

Figure 6.20 Reconstructed momentum (in GeV) of K_S^0 candidates (a) momentum of K_S^0 with (b) in x-direction; (b) y-direction (c) in z-direction

Figure 6.20 Reconstructed momentum (in GeV) of K_S^0 candidates (a) momentum of K_S^0 with (b) in x-direction; (b) y-direction (c) in z-direction

Figure 6.21 Two dimensional plot of mass (GeV) vs $\cos\vartheta$ of K_S^0 at pseudorapidity $-2 < \eta < 2$ (ϑ as the polar angle of K_S^0)

Figure 6.22 Reconstructed mass of $\phi(1020)$ from $\phi(1020) \rightarrow K_L^0 K_S^0$ channel (a) $\phi(1020)$ mass from $m(\phi(1020)) \rightarrow m(K_L^0 K_S^0)$; (b) an expansion of Figure (a); (c) Statistical error of the reconstructed $\phi(1020)$ mass from $\phi(1020) \rightarrow K_L^0 K_S^0$ channel. The invariant mass of $\phi(1020)$ is 1.019 GeV [35]

Figure 6.23 Reconstructed masses (in GeV) of (a) K_L^0 candidates using the ZUFOs entries; (b) mass K_S^0 candidates from V0 entries narrowed to $abs(Mass(\pi^+ \pi^-) - Mass(K_S^0)) < 0.02$.

Figure 6.24 Comparison of mass of $\phi(1020)$ reconstructed mass in GeV (dash line) against its mass from Monte Carlo simulation (solid line)

Figure 6.25 Comparison $\phi(1020)$ momentum (in GeV) (a) measured; (b) corrected; (c) simulated from Monte Carlo and matched in against measured momentum

Figure 6.26 Comparison of (a) efficiency; (b) purity; (c) acceptance of momentum of $\phi(1020)$ candidates versus energy (in GeV)

Figure 6.27 Differential cross section (in pb/GeV) of $\phi(1020)$ candidates with respect to its measured momentum (in GeV)

- Figure 6.28** Cosine azimuthal angle $\cos\vartheta$ of $\phi(1020)$
- Figure 6.29** Two dimensional plot of mass $\phi(1020)$ (GeV) vs $\cos\vartheta$ of K_L^0 at pseudorapidity $-2 < \eta < 2$ (ϑ as the polar angle K_L^0)
- Figure 6.30** Two dimensional plot of mass $\phi(1020)$ (GeV) vs $\cos\vartheta$ of K_S^0 at pseudorapidity $-2 < \eta < 2$ (ϑ as the polar angle of K_S^0)
- Figure 6.31** Two dimensional plot of K_L^0 mass (in GeV) vs. $\phi(1020)$ mass (in GeV)
- Figure 6.32** Two dimensional plot of K_S^0 mass (in GeV) vs. $\phi(1020)$ mass (in GeV)
- Figure 6.33** Comparison of ZUFOS energy $zufo(4,i)$ (in GeV) for object- i not associated with any track (solid line) against its background signal (dash line) for neutron candidates; (b) the background signal is curve fitted using function $e^{(a+b*zufo(4,i))}$ and is then used to isolate the ZUFOS energy of K_L^0 candidates from its background signal.
- Figure 6.34** Four-momentum (in GeV) from ZUFOS entry for object- i not associated with any track used in neutron reconstruction (a) Energy component (b) x-component (c) y-component (d) z-component
- Figure 6.35** Reconstructed four-momentum (in GeV) of neutron candidates (a) Energy component (b) x-component (c) y-component (d) z-component
- Figure 6.36** Cosine polar angle of K_L^0 candidates (a) measured $\cos\theta$ and (b) $\cos\theta$ from Monte Carlo simulation

Figure 6.37 Properties of reconstructed neutron candidates (a) $\delta_i = E_i - p_{zi}$ (in GeV); (b) centre-of-mass $W_{JB} = \sqrt{y_{JB} s}$ for the intermediate boson-proton ; (c) pseudorapidity η

Figure 6.38 Reconstructed mass of neutron candidates in GeV (a) mass of neutron constructed from ZUFO objects not associated with any tracks (b) an expansion of Figure (a); (c) neutron mass with errors (d) neutron from Monte Carlo simulation. The invariant mass of neutron is 0.939GeV [35].

Figure 6.39(a) Two dimensional plot of neutron mass (GeV) vs azimuthal angle θ (rad) of neutron

Figure 6.40 Comparison of momentum of neutron candidates (a) measured (b) matched in magnitude and direction against the ones from generated from Monte Carlo; (c) corrected

Figure 6.41 Comparison of (a) efficiency; (b) purity; (c) acceptance of momentum of neutron candidates

Figure 6.42 Differential cross section (in pb/GeV) of neutron candidates with respect to its measured momentum (in GeV)

Figure 6.43 Reconstructed momentum (in GeV) of $\gamma\gamma$ candidates from $\pi^0 \rightarrow \gamma\gamma$ decay channel (a) momentum (b) momentum in x-direction (c) momentum in y-direction (d) momentum in z-direction

Figure 6.44 Properties of $\pi^0 \rightarrow \gamma\gamma$ candidates: (a) mass of π^0 in GeV narrowed to $0.133 < \sqrt{E_{\gamma\gamma}^2 - p_{\lambda\gamma}^2} < 0.137$; (b) $\gamma\gamma$ energy in GeV; (c) $\gamma\gamma$ transverse momentum in GeV (c) $\cos\theta$ polar angle of $\gamma\gamma$

Figure 6.45 Reconstruction of Λ mass (in GeV) from $\Lambda \rightarrow n\pi^0$ channel (a) mass of Λ constructed from $m(\Lambda) \rightarrow m(n\pi^0)$ (b) an expansion of Figure (a); (c) Λ mass with errors (d) Λ from Monte Carlo simulation. The invariant mass of Λ is 1.115 GeV [35].

Figure 6.46 Comparison $\phi(1020)$ momentum (in GeV) (a) measured; (b) corrected; (c) simulated from Monte Carlo and matched in against measured momentum

Figure 6.47 Comparison of (a) purity (b) efficiency; (c) acceptance of momentum of Λ candidates versus energy (in GeV)

Figure 6.48 Differential cross section of neutron candidates with respect to its measured momentum momentum (pb/GeV) vs its energy (in GeV).

List of Tables

Table 2.1 Components of $\Lambda \rightarrow n\pi^0$ channel

Table 2.2 Components of $\phi \rightarrow K_L^0 K_S^0$ channel

Table 3.1 Properties of ZEUS CAL listed by section

Table 3.2 Centre radius of superlayers in the CTD of ZEUS detector [1]

Table 4.1 Some of the output label from FPGA-based readout control (ROC) as shown in Figure 4.4 (a) and its status

Table 4.2 Thermal dissipation of readout control block